

---

# Bayesian Scattering: A Principled Baseline for Uncertainty on Image Data

---

Bernardo Fichera<sup>1</sup> Zarko Ivkovic<sup>2</sup> Kjell Jorner<sup>2</sup> Philipp Hennig<sup>1</sup> Viacheslav Borovitskiy<sup>3</sup>

## Abstract

Uncertainty quantification for image data is dominated by complex deep learning methods, yet the field lacks an interpretable, mathematically grounded baseline. We propose *Bayesian scattering* to fill this gap, serving as a first-step baseline akin to the role of Bayesian linear regression for tabular data. Our method couples the wavelet scattering transform—a deep, non-learned feature extractor—with a simple probabilistic head. Because scattering features are derived from geometric principles rather than learned, they avoid overfitting the training distribution. This helps provide sensible uncertainty estimates even under significant distribution shifts. We validate this on diverse tasks, including medical imaging under institution shift, wealth mapping under country-to-country shift, and Bayesian optimization of molecular properties. Our results suggest that Bayesian scattering is a solid baseline for complex uncertainty quantification methods.

## 1. Introduction

Uncertainty estimates are crucial for automated decision-making, safety-critical applications, and more (Abdar et al., 2021; Gawlikowski et al., 2023). Yet, deep learning methods, while highly accurate, often fail to deliver useful uncertainty estimates, especially under distribution shift—when test-time inputs differ substantially from the training ones (Gustafsson et al., 2023; Koh et al., 2021).<sup>2</sup>

Furthermore, although recent breakthroughs in machine learning have largely been enabled by massive datasets and ever-larger models, many problems in domains of growing importance—such as scientific and medical applications—lack the luxury of abundant data. While transfer learning and foundation models offer a potential remedy, they in-

roduce new complexities regarding safety, robustness, and uncertainty calibration (Awais et al., 2025; Bommasani et al., 2021). We argue that this increasing complexity necessitates interpretable baselines to anchor empirical evaluation and clarify the true benefits of more complex approaches. Establishing such a baseline for image data is the main objective of this paper.

We propose the *scattering transform* (Bruna and Mallat, 2013) as the foundation for such a baseline. Scattering transforms produce deep, hierarchical feature maps that are provably translation-invariant and stable to small deformations and additive noise (Mallat, 2010). These properties explicitly encode the geometric inductive biases of natural images—biases that convolutional neural networks and vision transformers must otherwise acquire through massive pretraining (Dosovitskiy et al., 2020). This grounding makes the scattering transform a principled choice, while its nature as a fixed, non-learned feature extractor ensures it cannot overfit the training distribution, thereby offering inherent robustness to distribution shift. Its effectiveness as a powerful feature extractor has been demonstrated in computer vision—particularly in data-scarce regimes (Gauthier et al., 2022; Oyallon et al., 2018)—and in scientific modeling tasks (Eickenberg et al., 2017; Hirn et al., 2017).

Despite this record, the potential of scattering transforms for uncertainty quantification has been largely overlooked. To fill this gap, we propose *Bayesian scattering*, which combines scattering features with a simple probabilistic head such as a Gaussian process (Rasmussen and Williams, 2006), as illustrated in Figure 1. We describe how this method arises from the geometry of the image space and discuss its main properties. By coupling a principled, geometry-motivated feature extractor—immune to overfitting by design—with a simple probabilistic head, we create an interpretable and robust reference model. Crucially, it is not intended to claim state-of-the-art performance, but rather to constitute a principled baseline for evaluating more complex approaches. Such a baseline is particularly important in uncertainty quantification, where scalar metrics may be insufficient to guarantee safety or downstream utility, necessitating a reference model that is grounded by design rather than merely optimized for a specific score.

<sup>2</sup>In this paper, *distribution shift* refers to *covariate shift*: when the input distribution changes while the conditional remains fixed.

Code available at: [github.com/nash169/bayesian-scattering](https://github.com/nash169/bayesian-scattering)  
<sup>1</sup>University of Tübingen <sup>2</sup>ETH Zurich <sup>3</sup>University of Edinburgh.  
 Correspondence to: B. Fichera <bernardo.fichera@gmail.com>, V. Borovitskiy <viacheslav.borovitskiy@gmail.com>.

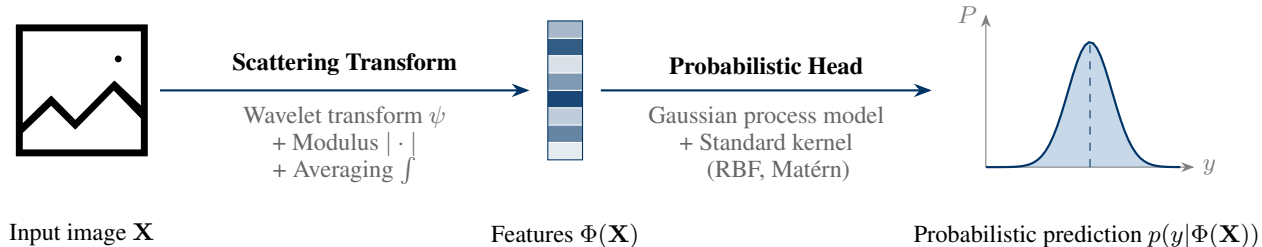


Figure 1. Bayesian scattering maps an input image  $\mathbf{X}$  to a probabilistic prediction  $p(y | \Phi(\mathbf{X}))$  via the scattering features  $\Phi(\mathbf{X})$ .

In our experiments, we focus on regression, as it allows exact Gaussian process inference in small data settings, thereby minimizing confounding factors in method evaluation. To provide practical guidelines, we first conduct a preliminary study in a simple, stylized setting (QM2D dataset of Hirn et al. (2017)), analyzing hyperparameter sensitivity and feature behavior. We then demonstrate the method’s efficacy on diverse tasks with realistic distribution shifts, including two medical imaging settings with institution shifts (Gustafsson et al., 2023), as well as wealth mapping (Koh et al., 2021; Yeh et al., 2020) under a country-to-country shift. Finally, we validate the utility of the baseline in downstream decision-making via Bayesian optimization of molecular properties on the QM2D and QM9 datasets (Ramakrishnan et al., 2014; Ruedigke et al., 2012).

## 2. Related Work

**Uncertainty for images.** The standard approach to uncertainty quantification for images involves modifying or post-processing deep neural networks. Prominent methods include deep ensembles (Lakshminarayanan et al., 2017), which average predictions over multiple independently trained models; Monte Carlo dropout (Gal and Ghahramani, 2016), which approximates Bayesian inference via dropout at test time; and scalable Laplace approximations (Daxberger et al., 2021), which estimate the posterior curvature around a MAP solution. While effective, these methods rely on learned feature representations that can be opaque and prone to overconfidence under distribution shift (Gustafsson et al., 2023; Ovadia et al., 2019). Hybrid approaches like deep kernel learning (Wilson et al., 2016) or other combinations of neural networks and Gaussian processes (Bradshaw et al., 2017) attempt to mitigate this by placing probabilistic heads on top of deep networks. However, they still inherit the data-hunger and biases of the underlying learned features.

**Scattering transforms and applications.** The scattering transform (Bruna and Mallat, 2013) has been proposed as a robust feature extractor for small-data regimes in image classification (Oyallon et al., 2018) and scientific modeling (Eickenberg et al., 2017; Hirn et al., 2017). While sev-

eral engineering studies have technically combined scattering features with Gaussian processes (Ferkous et al., 2021; Lone and Aydin, 2023; Ojha et al., 2024; Sudirman et al., 2022), they do not constitute a precedent for the baseline we propose. Crucially, most of these works (Ferkous et al., 2021; Lone and Aydin, 2023; Sudirman et al., 2022) utilize the Gaussian process solely for kernel regression (predicting the mean) and omit uncertainty quantification entirely. The only exception (Ojha et al., 2024) considers uncertainty but is restricted to time series rather than image data and concentrates on the specific application of impact localization. To our knowledge, no prior work has proposed or explicitly evaluated Bayesian scattering as a robust baseline for uncertainty quantification on image data.

## 3. Scattering

We now introduce *wavelet scattering transforms*, or simply *scattering transforms*, which form the backbone of the principled baseline we propose. We begin by reviewing the fundamental properties desirable for any feature representation of images. These properties, which capture the geometric inductive biases of natural images, constitute the defining characteristics of scattering transforms. We then detail the construction of the transform from cascades of *linear wavelet transforms*, pointwise *nonlinearities*, and *pooling* by (local) averaging. Finally, we discuss the integration of rotation invariance in scattering transforms and the dimensionality of the resulting scattering feature maps.

### 3.1. Defining Properties of Scattering Transforms

To motivate scattering transforms, we first discuss the general properties that any “good” feature map for images should satisfy. For simplicity, let us neglect the discrete nature of images for a while and treat them as functions  $f : \mathbb{R}^2 \rightarrow \mathbb{R}$ . Let  $\Phi : L^2(\mathbb{R}^2) \rightarrow \mathcal{H}$  denote our feature map.

First, since shifting an image does not change its semantic content, the feature map  $\Phi$  should satisfy

1. **Translation-invariance:**  $\Phi(T_c f) = \Phi(f)$  where we have  $f \in L^2(\mathbb{R}^2)$ ,  $c \in \mathbb{R}^2$ , and  $T_c f(x) = f(x - c)$ .

Translation-invariance (Figure 2a) is important, being a key inductive bias of convolutional neural networks.<sup>1</sup>

Can we further simplify the feature space by demanding invariance to a broader class of transformations? Deformations—formally,  $C^2$ -diffeomorphisms  $\tau : \mathbb{R}^2 \rightarrow \mathbb{R}^2$  which act on  $f : \mathbb{R}^2 \rightarrow \mathbb{R}$  via  $(D_\tau f)(\mathbf{x}) = f(\tau(\mathbf{x}))$ —form a much richer group than translations. However, invariance to all such deformations would eliminate essential information, as illustrated in Figure 2c. A more appropriate requirement is *stability to small deformations*: small, smooth input variations should yield only small changes in the feature representation. This property is formalized as

2. **Stability to small deformations:** for all  $f \in L^2(\mathbb{R}^2)$  and for all  $C^2$ -diffeomorphisms  $\tau$  with  $\|\tau - \text{id}\| \leq 1$ , it is true that  $\|\Phi(D_\tau f) - \Phi(f)\| \leq C\|f\|\|\tau - \text{id}\|$ . Here,  $\text{id}(\mathbf{x}) = \mathbf{x}$  is the identity;  $C > 0$  is a constant.

In addition to deformation stability, a feature map should naturally be stable to additive noise (see Figure 2b):

3. **Stability to additive noise:** for all  $f, \varepsilon \in L^2(\mathbb{R}^2)$  and some  $C > 0$ , we have  $\|\Phi(f + \varepsilon) - \Phi(f)\| \leq C\|\varepsilon\|$ .

Finally, the feature map must be *rich* enough for downstream learning: it should not eliminate crucial information or collapse semantically meaningful distinctions. Ideally, one seeks features that are as informative as possible, potentially invertible up to invariances such as translation.

Constructing feature maps that are simultaneously invariant, stable, and expressive turns out to be a highly nontrivial task. Naïve approaches often succeed in only one or two of these aspects, but not all of them simultaneously. *Wavelet scattering transforms* are specifically designed to address this challenge. For a discussion of typical failure modes in naïve approaches and further motivation, see Appendix A.

### 3.2. Explicit Construction

This section provides an explicit construction of scattering transforms, focusing on the concrete steps and intuition most relevant for practical applications. For clarity and brevity, we deliberately omit a number of important technical assumptions, as well as subtleties concerning convergence and normalization. All of these are rigorously addressed in Bruna and Mallat (2013) and Mallat (2012).

**Wavelets** We start by fixing a family of “nice” complex-valued *wavelets*  $\psi_{j,r} : \mathbb{R}^2 \rightarrow \mathbb{C}$ , where  $j \in \mathbb{Z}$  encodes the

<sup>1</sup>Although the convolutions themselves are *equivariant* (Cohen and Welling, 2016), the presence of subsampling—e.g., as a result of pooling—in traditional architectures leads to (local) invariance. As discussed later in the paper, scattering transforms can also be made to exhibit local, rather than global, invariance.

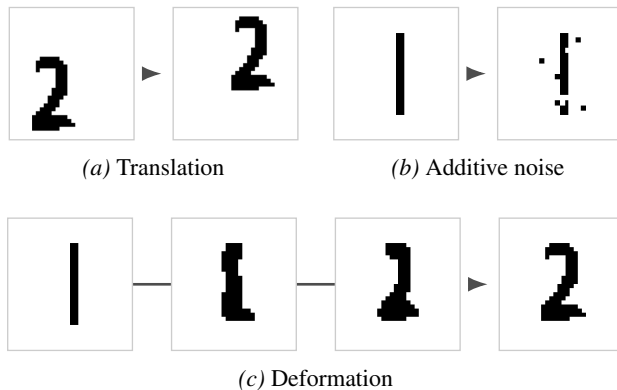


Figure 2. Different types of transformations that feature maps should be invariant or stable to. Note: while single steps in (c) are small deformations, their composition changes the image content.

scale and  $r$  indexes a finite group  $R \subset O(2)$  of rotations and reflections. These are simple waveforms, localized both in frequency and spatial domains, chosen so that their Fourier transforms  $\widehat{\psi_{j,r}}$  cover the whole frequency domain. Then, the *wavelet transform* maps  $f$  to  $\{W[j,r]f\}_{j \in \mathbb{Z}, r \in R}$ , where  $W[j,r]f = f * \psi_{j,r}$ . Each  $\psi_{j,r}$  is a convolutional filter, but here it is analytically defined rather than learned.

**Translation-invariant scattering transform** To build rich representations, Mallat (2012) proposed to combine wavelet transforms with nonlinearities—specifically, with the complex modulus  $|\cdot|$ , leading to  $U[j,r]f = |W[j,r]f|$ , and then cascade these  $U[j,r]$ , building deep representations. For a *path*  $p = ((j_1, r_1), \dots, (j_m, r_m))$  this leads to the definition of the *scattering propagator*  $U[p]$ :

$$U[p]f = U[j_m, r_m] \dots U[j_1, r_1]f \quad (1)$$

Each  $U[p]$  is stable to additive noise and small deformations (Mallat, 2012). Furthermore, the collection  $\{U[p]f\}_p$  is maximally expressive, allowing recovery of  $f$ . However,  $U[p]$  is not translation-invariant—rather, it is translation-equivariant (Mallat, 2012). Furthermore, it is overly redundant and impractical to work with, being an infinite collection of functions. The *translation-invariant scattering transform* maps  $f$  to  $\{S[p]f\}_p$  where  $S[p]f : L^2(\mathbb{R}^2) \rightarrow \mathbb{R}$  is built from  $U[p]$  by averaging—in the context of neural networks, a form of pooling—of the scattering propagator:

$$S[p]f = \int_{\mathbb{R}^2} U[p]f(\mathbf{x}) d\mathbf{x} \in \mathbb{R} \quad (2)$$

In practice, one chooses a finite set of paths  $P$ —we discuss the choice in Sections 3.4 and 4.2—and only computes  $S_P f = \{S[p]f\}_{p \in P} \in \mathbb{R}^{|P|}$ . It is guaranteed to satisfy all the properties from Section 3.1 (Bruna and Mallat, 2013).

**Windowed scattering transform** Sometimes it may be desirable to only retain invariance to *small* translations,

say only to translations by  $\|c\| \lll 2^J$ ,  $J \in \mathbb{N}$ . This is achieved by the *windowed scattering transform*  $S^w$ . It replaces global averaging with a localizing convolution,

$$S^w[p]f = U^w[p]f * \phi_{2^J}, \quad \phi_{2^J}(\mathbf{x}) = 2^{-dJ} \phi(2^{-J} \mathbf{x}), \quad (3)$$

where  $\phi$  is a smooth, rapidly-decaying bump function (e.g., a Gaussian). Importantly, unlike  $S[p]$ , which outputs a scalar,  $S^w[p]$  outputs a function which in practice has to be discretized. To preserve the properties 2 and 3 from Section 3.1, the propagator  $U^w$  should be redefined by restricting onto paths with  $j \leq J$  and allowing the averaging  $f * \phi_{2^J}$  to be used alongside any  $U[j, r]f$  in Equation (1).

### 3.3. Rotation Invariance

Whether rotation invariance is desirable for a feature map depends on the task: for example, it is not always appropriate in digit recognition (e.g., a 6 rotated by  $180^\circ$  resembles a 9), but important for predicting molecular properties from approximate electronic density images of arbitrary orientation. With a suitable wavelet design, scattering transforms are *equivariant* to rotations (Eickenberg et al., 2017; Hirn et al., 2017). In this case, a rotation-invariant propagator  $S^{\text{rot-inv}}[(j_1, \dots, j_m)]$  can be obtained by averaging:

$$\frac{1}{|R|^m} \sum_{r_m \in R} \cdots \sum_{r_1 \in R} S[(j_1, r_1), \dots, (j_m, r_m)]f. \quad (4)$$

### 3.4. Feature Map Dimensionality

The expressiveness of scattering features depends on the number and structure of retained paths. Mallat (2012) and Waldspurger (2017) show that  $|S[p]f|$  decay exponentially with path length  $m$ . It thus suffices to restrict to short paths, typically  $m \leq 2$  or 3. Moreover, only paths with  $j_1 < \dots < j_m$  and  $1 \leq j_i \leq J$  are really needed, where  $J$  is a hyperparameter with  $2^J \leq N$  for discrete images of size  $N \times N$ . There are  $|R|^m \binom{J}{m}$  paths of length  $m$ , so truncating at  $m \leq M$  gives  $\sum_{m=1}^M |R|^m \binom{J}{m}$  features. For windowed scattering, this total is multiplied by the output resolution, typically  $N^2/2^{2J}$  for  $N \times N$  images. With rotation invariance (Equation (4)), the  $|R|^m$  factors drop out.

## 4. Bayesian Scattering

We now formalize *Bayesian scattering*, a framework that pairs the fixed, principled features of the scattering transform with a simple probabilistic head. The core premise is that while simple probabilistic models—such as Gaussian processes—excel on tabular data, they are ill-suited for the high dimensionality and complex geometry of raw images. The scattering transform bridges this gap: it reduces dimensionality and filters irrelevant variation, projecting images into a structured feature space where the Euclidean

metric aligns with semantic content better. This mirrors the simplification of learned representations, but with a key advantage: because scattering features are not optimized on the training set, they remain independent of the training distribution. This decoupling avoids overfitting and fosters robust uncertainty estimation even under distribution shift.

### 4.1. General Framework

Consider a dataset  $\mathcal{D} = \{(\mathbf{X}_i, y_i)\}_{i=1}^n$ , where inputs  $\mathbf{X}_i$  lie in pixel space  $\mathcal{I} = \mathbb{R}^{N \times N}$  and outputs  $y_i \in \mathcal{Y}$  represent targets (e.g.,  $\mathcal{Y} = \mathbb{R}$  for regression,  $\mathcal{Y} = \{0, \dots, C-1\}$  for classification).<sup>2</sup> Let  $\Phi : \mathcal{I} \rightarrow \mathbb{R}^M$  be the fixed scattering feature map. We define a probabilistic model over the target  $y$  given the transformed input via some latent function  $f$ :

$$y \mid \mathbf{X}, f \sim p(y \mid f(\Phi(\mathbf{X}))), \quad (5)$$

where  $p(y \mid \cdot)$  is an appropriate likelihood. By placing a prior  $p(f)$  over functions on the feature space  $\mathbb{R}^M$ , we effectively induce a prior  $f^\Phi(\mathbf{X}) := f(\Phi(\mathbf{X}))$  on the original pixel space  $\mathcal{I}$ . Given the dataset  $\mathcal{D}$ , the posterior distribution over the latent function is  $p(f \mid \mathcal{D})$ , while the predictive for a new test point  $\mathbf{X}^*$  is obtained by marginalization:

$$p(y^* \mid \mathbf{X}^*, \mathcal{D}) = \int p(y^* \mid f(\Phi(\mathbf{X}^*))) p(f \mid \mathcal{D}) df. \quad (6)$$

This predictive distribution encapsulates both the deterministic prediction and uncertainty. For regression ( $\mathcal{Y} = \mathbb{R}$ ), the expectation  $\mathbb{E}[y^*]$  corresponds to the prediction, while the standard deviation  $\sqrt{\text{Var}[y^*]}$  quantifies uncertainty—intuitively, the estimated magnitude of the error. For classification, these correspond to the mode (predicted class) and the entropy of the distribution, respectively.

### 4.2. Instantiating the Framework

To instantiate this framework, we adhere to standard scattering conventions (Bruna and Mallat, 2013; Eickenberg et al., 2017; Hirn et al., 2017). First, we restrict to paths of length  $m \leq 2$ : deeper paths are typically unnecessary due to the exponential decay of feature energy and computationally prohibitive due to growth in feature dimensionality. Second, following the implementation in `Kymatio` (Andreux et al., 2020), when using the windowed scattering transform, we discretize the output with a stride of  $2^J$ , yielding a feature map of spatial resolution  $N/2^J \times N/2^J$ .

Within this setup—and assuming a wavelet family is fixed by the implementation—Bayesian scattering involves the following three modeling choices:

- Scattering invariances:** Use the fully translation-invariant transform  $S$  or its windowed version  $S^w$ ;

<sup>2</sup>For multi-channel images (e.g., RGB), scattering is applied to each channel independently; resulting features are concatenated.

whether to impose rotation-invariance using  $S^{\text{rot-inv}}$ .

2. **Scattering hyperparameters:** Number of scales  $J$  ( $2 \leq 2^J \leq N$ ), size of the discrete rotation group  $L = |R|$ —or similar in case of non-standard wavelets.
3. **Probabilistic head:** This includes the prior, which can come with hyperparameters to be fit from data, and the inference method for obtaining the posterior.

The choice between  $S$ ,  $S^w$ , and  $S^{\text{rot-inv}}$  is usually guided by the invariances inherent to the problem at hand. Moreover, scattering hyperparameters can typically be treated in the same way as the hyperparameters of the probabilistic head.

**Probabilistic head** To maintain the transparency of the baseline, we strongly recommend keeping the probabilistic head simple. Specifically, we advocate for Gaussian process (GP) regression or classification with standard covariance functions, such as the Matérn, RBF, or linear kernels (Rasmussen and Williams, 2006). Note that the latter choice recovers Bayesian linear or logistic regression. A standard advantage of Gaussian processes is the ability to perform model selection (e.g., kernel choice, or even choice of  $J$ ) by simply maximizing the *log marginal likelihood* on the training data. While this theoretically streamlines the workflow by removing the need for a validation set, we caution that it can lead to overfitting for the relatively high-dimensional feature spaces typical of scattering transforms.

### 4.3. Inference and Computation

Because the scattering feature map  $\Phi$  is fixed, feature extraction is strictly decoupled from the probabilistic modeling. This separation allows to move the data from the complex, high-dimensional pixel space  $\mathcal{I}$  into a more structured, moderate-dimensional vector space  $\mathbb{R}^M$ , effectively reducing the task to a standard probabilistic problem on tabular data. Consequently, the choice of inference method is dictated solely by computational constraints (dataset size  $N$ ) and the target task (likelihood  $p(y | \cdot)$ ).

**Feature extraction** Computationally, extracting scattering features is equivalent to a forward pass of a fixed convolutional network involving wavelets and smooth bump functions, as well as the modulus non-linearities. This process is highly efficient and amenable to standard GPU acceleration, supported by libraries such as `Kymatio` (Andreux et al., 2020), which handles both 2D images and their 3D counterparts. The resulting feature map dimension was discussed in Section 3.4. In practice, the dimensionality of the scattering feature map usually falls between  $10^2$ – $10^4$ .

**Exact inference** For regression tasks on moderate-sized datasets ( $N$  of order  $10^3$ ), we recommend exact Gaussian

process regression. In this regime, the learning problem reduces to standard Gaussian process regression on transformed inputs  $\mathbf{x}_i = \Phi(\mathbf{X}_i) \in \mathbb{R}^M$ . This approach provides a “gold-standard” baseline devoid of inference-level approximation errors, where the posterior mean and variance are computed via Cholesky decomposition with  $\mathcal{O}(N^3)$  complexity (Rasmussen and Williams, 2006). Crucially, the log marginal likelihood can be computed exactly with the same complexity, further streamlining model selection.

**Variational inference** To scale to larger  $N$ , or to handle the non-Gaussian likelihoods required for classification, one can employ approximate inference. Specifically, the stochastic variational Gaussian process (SVGP) framework of Hensman et al. (2013) introduces a set of *inducing inputs*  $Z \subset \mathbb{R}^M$  and corresponding *inducing variables*  $\mathbf{u} = f(Z)$ . The joint posterior is approximated by a variational distribution with the structure  $q(f, \mathbf{u}) = p(f | \mathbf{u})q(\mathbf{u})$ . The parameters of  $q(\mathbf{u})$  are learned by maximizing the evidence lower bound (ELBO), which factorizes over the data:

$$\sum_{i=1}^N \mathbb{E}_{f \sim q(f)} \log p(y_i | f(\mathbf{x}_i)) - \text{KL}[q(\mathbf{u}) || p(\mathbf{u})]. \quad (7)$$

This factorization enables mini-batch training similar to standard deep learning and reduces complexity to  $\mathcal{O}(|Z|^3)$  where  $|Z| \ll N$ . Such flexibility enables Bayesian scattering to be used for large-scale or classification tasks.

## 5. Experiments

We evaluate Bayesian scattering across three distinct regimes to validate its utility as a robust baseline. First, we conduct a sensitivity analysis in a controlled setting to establish best practices and understand hyperparameter trade-offs. Second, we assess performance under real-world distribution shifts using three diverse regression benchmarks: histology, skin lesion analysis, and satellite-based wealth prediction. Finally, we investigate the utility of the method for downstream decision-making via Bayesian optimization of molecular properties.

### 5.1. Sensitivity Analysis and Best Practices

Before addressing distribution shifts, we conduct a preliminary study to establish practical guidelines for Bayesian scattering. We focus on `QM2D`, a dataset of 4,357 planar molecules derived from the standard `QM7` dataset (Blum and Reymond, 2009; Rupp et al., 2012). Following Hirn et al. (2017), we represent each molecule as a 2D image with three channels: valence electronic density, core electronic density, and “Dirac”—in Figure 3 (b) we visualize these as RGB images. While this task does not involve distribution shift, it serves as a controlled test for understanding hyperparameter sensitivity and computational trade-offs. De-

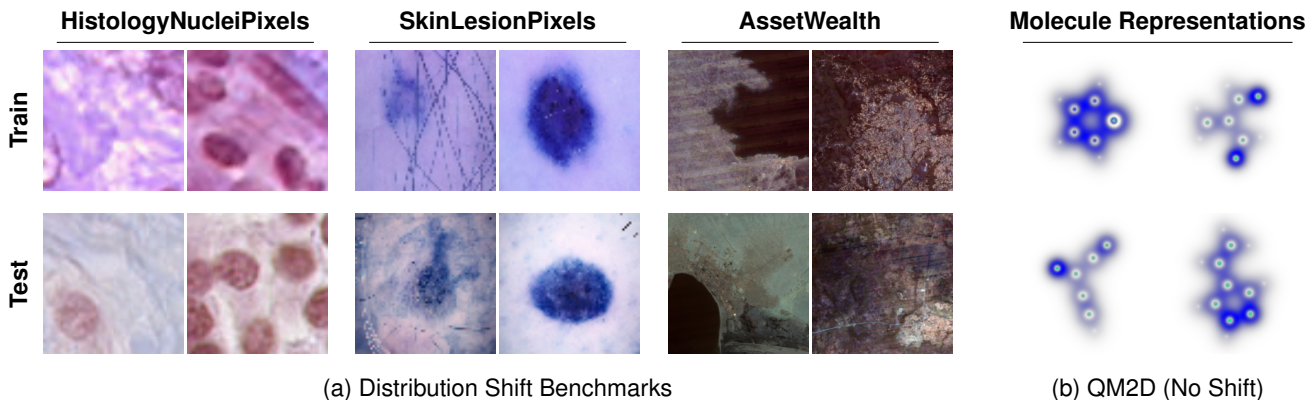


Figure 3. Datasets used in Section 5 with the exception of QM9 whose 3D image representations are difficult to visualize.

tailed results are in Appendix B; here we summarize the key takeaways that inform our subsequent experiments.

**Scattering configuration** We study the impact of the number of scales  $J$  and the number of angular orientations  $L = |R|$  (the size of the rotation group). Here, we consistently found that  $L = 8$  provides the optimal balance between performance and computation; increasing  $L$  beyond this point yielded no performance gains. For the scaling parameter,  $J \approx \log_2 N - 1$  (where  $N$  is as in  $N \times N$  resolution image) proved optimal across resolutions. This suggests that, in practice, retaining some local translation sensitivity may be beneficial compared to the full global averaging ( $J = \log_2 N$ ) even for fully translation-invariant tasks.

**Feature dimensionality reduction** Contrary to common practice in scattering literature (Bruna and Mallat, 2013), we found that applying principal component analysis (PCA) to scattering features—even when keeping 100% of variance—often degraded both calibration and accuracy. We hypothesize that the rotation of the feature space disrupts its geometric structure, resulting in a representation less aligned with the priors induced by standard kernels. Furthermore, truncating the basis to retain only partial variance can be detrimental for uncertainty quantification under distribution shift, as it may discard features that are latent in the training distribution but vital for generalization. We thus recommend using raw scattering features.

**Kernel choice and ARD** The parameter-free linear kernel frequently exhibited numerical instability in our experiments; we therefore recommend standard RBF or Matérn kernels. While automatic relevance determination (ARD) kernels (MacKay, 1992; Rasmussen and Williams, 2006) can improve the flexibility of the model by learning per-feature lengthscales, we found them prone to overfitting as feature dimensionality grows. For this reason, we recommend ARD kernels primarily for lower-dimensional feature maps (e.g., when rotation-invariance or full translation-

invariance is imposed) and advise exercising caution when applying them to higher-dimensional representations.

**Optimization and efficiency** For exact Gaussian process inference, we found that optimizing the log marginal likelihood for 500 iterations using Adam (Kingma, 2014) provides a robust trade-off between convergence and cost. To ensure numerical stability, we recommend initializing lengthscales to the mean pairwise distance of the training features. In terms of wall clock time, feature extraction for QM2D (at  $J = 7, L = 8$ ) took approximately 876 seconds with rotation invariance and 1236 seconds without; we attribute the latter’s increased runtime to implementation specifics. Compared to the 790 seconds required for a small 3.7M parameter CNN (ConvNeXt-Atto) on the same hardware, these results demonstrate that Bayesian scattering is competitive with small deep learning models.

## 5.2. Image Regression

We now evaluate Bayesian scattering on a set of regression tasks with real-world distribution shifts.

**Datasets** We focus on three datasets from the benchmarks of Gustafsson et al. (2023) and Koh et al. (2021) whose sample inputs we visualize in Figure 3 (a). These are

- **SkinLesionPixels** (SLP) (Gustafsson et al., 2023): Medical imaging task. The goal is to predict the count of lesion pixels in a  $64 \times 64$  dermatoscopic image. It is based on the HAM10000 dataset by Tschandl et al. (2018) which consists of different sub-datasets, the training set (6,592 images) was collected in Austria while the test (2,259) was collected in Australia, with different equipment and skin type distribution.
- **HistologyNucleiPixels** (HP) (Gustafsson et al., 2023): Medical imaging task. The goal is to predict the count of nuclei pixels in  $64 \times 64$  histology crops. The shift is *institutional*: the training set (10,808 im-

Table 1. Performance comparison on image regression tasks under real-world distribution shifts. We report the mean and standard deviation across 5 synchronized random splits. The best result is underlined; results not statistically significantly different are **bolded**.

Data	Metric	Trivial	Ensemble (5x ConvNeXt-Atto)	Scattering	ConvNeXt		DINOv2	
					Atto	Base	Small	Base
SLP	RMSE	815 ± 34	626 ± 29	<b>543 ± 28</b>	<u>541 ± 40</u>	<b>558 ± 21</b>	783 ± 39	730 ± 34
	NLL	1.52 ± 0.06	12.49 ± 3.5	<b>1.35 ± 0.19</b>	1.62 ± 0.27	<u>1.24 ± 0.11</u>	1.87 ± 0.15	1.80 ± 0.23
	QCE	0.03 ± 0.02	0.49 ± 0.05	0.14 ± 0.02	0.14 ± 0.02	<u>0.08 ± 0.02</u>	0.14 ± 0.01	0.14 ± 0.02
	PI- $\mu$	3.92 ± 0.00	0.65 ± 0.05	<u>1.62 ± 0.08</u>	<b>1.64 ± 0.10</b>	2.24 ± 0.18	2.65 ± 0.09	2.59 ± 0.15
	PI- $\sigma$ ↑	0.00 ± 0.00	0.43 ± 0.05	0.64 ± 0.05	0.50 ± 0.06	0.30 ± 0.02	1.14 ± 0.13	1.26 ± 0.09
HP	RMSE	635 ± 19	475 ± 13	<b>392 ± 46</b>	490 ± 50	513 ± 26	<b>447 ± 48</b>	<b>447 ± 24</b>
	NLL	1.33 ± 0.04	11.00 ± 3.21	<u>0.82 ± 0.07</u>	<b>0.88 ± 0.09</b>	0.96 ± 0.09	<b>0.89 ± 0.14</b>	<b>0.84 ± 0.10</b>
AW	RMSE	0.90 ± 0.02	0.63 ± 0.04	0.64 ± 0.03	<b>0.57 ± 0.04</b>	<b>0.56 ± 0.03</b>	<b>0.53 ± 0.03</b>	<b>0.53 ± 0.02</b>
	NLL	1.54 ± 0.03	7.77 ± 0.88	1.06 ± 0.05	<b>0.98 ± 0.07</b>	<b>0.98 ± 0.07</b>	<u>0.92 ± 0.06</u>	<b>0.93 ± 0.05</b>

ages) is derived from CONNSEP (Graham et al., 2019) data, while the test (2,267) comes from TNBC (Naylor et al., 2018), created by a different institution with inherent variations in staining and sample preparation.

- **AssetWealth (AW)** (Koh et al., 2021; Yeh et al., 2020): Wealth mapping task using 8-channel satellite images to predict an asset wealth index for locations across 23 African countries. We resize the original  $224 \times 224$  inputs to  $256 \times 256$  for compatibility with standard architectures. The setup defines a challenging distribution shift by splitting data based on country: the training set (11,797 images) and test set (3,963 images) are drawn from disjoint lists of nations. This introduces significant variation, as both the terrain and the visual markers of wealth differ across regions.

**Metrics** We report the negative log likelihood (NLL) to assess the joint quality of prediction and uncertainty. Furthermore, to disentangle these aspects, we also report root mean squared error (RMSE) for predictive accuracy, quantile coverage error (QCE) to evaluate calibration, as well as mean and standard deviation of prediction interval width (PI- $\mu$  and PI- $\sigma$ ) to evaluate sharpness and dispersion—see Tran et al. (2020) for definitions.

**Setup** To simulate critical data-scarce regimes, we randomly subsample training and test sets to  $N_{\text{train}} = 1000$  and  $N_{\text{test}} = 250$ . This protocol enables robust evaluation

Table 2. Ablation study on SkinLesionPixels (mean over 5 runs). We compare rotation-invariant Bayesian scattering (BS-RI) across scales  $J$  and kernels (RBF ± ARD) against deep ensembles trained on scattering features and raw ConvNeXt features.

Metric	BS-RI ( $J = 3$ )		BS-RI ( $J = 5$ )		Ensemble	
	RBF	RBF-A	RBF	RBF-A	Scatt.	NN
Train Loss	0.65	<b>0.60</b>	0.74	0.68	-	-
RMSE	543	542	584	583	<b>512</b>	524
NLL	<b>1.34</b>	1.37	1.78	2.0	18.6	37.8

across five randomized, synchronized splits. We benchmark Bayesian scattering ( $L = 8$ ) against exact GP regression on features from state-of-the-art pre-trained models: ConvNeXt (Atto 3.7M, Base 88M) and DINOv2 (Small 22M, Base 88M). For the 8-channel AssetWealth data, we adapt these RGB models by processing channels independently and concatenating the outputs. To contextualize these against a standard learned baseline, we also evaluate a deep ensemble of five ConvNeXt-Atto models trained end-to-end. We selected the Atto variant as its smaller parameter count is the most appropriate for our data-scarce regime. GP hyperparameters are optimized via log marginal likelihood; we report statistics for the best-performing configuration (kernel type, ARD, scale  $J$ , rotation-invariance) for each method.

**Results** The main results are summarized in Table 1. Remarkably, all methods employing fixed features with a GP head drastically outperform the end-to-end deep ensemble across all metrics. On HP, Bayesian scattering achieves top-tier performance, matching or exceeding the learned features in both accuracy (RMSE) and likelihood (NLL) while offering superior calibration. On SLP, it remains highly competitive, outperforming DINOv2 and rivaling ConvNeXt. Crucially, detailed analysis (see Appendix B) reveals that scattering models here are “selectively uncertain”—producing prediction intervals that vary significantly in width depending on input difficulty—whereas neural baselines tend to output more static intervals. Finally, on the AW task, while scattering lags behind deep models in raw predictive error, it maintains robust calibration (QCE) comparable to the competition. This confirms that even when fixed geometric features limit predictive accuracy, the Bayesian scattering framework can still obtain reliable uncertainty.

### 5.2.1. MORE DATA AND APPROXIMATE INFERENCE

To demonstrate scalability, we evaluate performance on the full SLP training set ( $N = 6,592$ ) using SVGP (Hensman

et al., 2013) inference with  $|Z| = 1024$  inducing points and mini-batch training.

Results (see Appendix B, Table 3) confirm that the trends observed in the data-scarce regime persist at a larger scale. While predictive accuracy naturally improves with more data, the primary benefit is significantly improved calibration (lower QCE and NLL). This suggests that Bayesian scattering can effectively leverage denser data coverage to refine its uncertainty estimates.

### 5.2.2. MODEL CHOICE AND DEEP ENSEMBLE HEADS

Finally, we perform an ablation study to isolate the impact of the probabilistic head and verify whether training marginal likelihood reliably predicts generalization under distribution shift. We benchmark the Gaussian process head against a deep ensemble of 5 MLPs (one hidden layer, 128 units) trained on the fixed scattering features.

Key results are summarized in Table 2. Hyperparameter sensitivity proves domain-dependent: while HP is virtually invariant to configuration changes (see Appendix B), SLP is sensitive to both scale  $J$  and the use of ARD. Regarding the probabilistic head, deep ensembles on scattering features yield competitive mean predictions (RMSE) on SLP but suffer from extreme overconfidence (high NLL) under distribution shift. They perform similarly to or worse than GPs on other datasets (Appendix B). Critically, we find that training marginal likelihood is a poor proxy for model selection here. For instance, ARD models on SLP achieve lower training loss but significantly higher test NLL compared to non-ARD kernels, highlighting the risk of overfitting when optimizing flexible lengthscales in high-dimensional geometric feature spaces.

### 5.3. Bayesian Optimization

We conclude our evaluation by applying Bayesian scattering to a downstream decision-making task: Bayesian optimization (BO) of molecular properties. This setting is directly relevant to scientific discovery, where uncertainty estimates can guide sequential selection of candidates to optimize a target property efficiently (Frazier, 2018).

**Planar molecules (QM2D)** We begin with the QM2D dataset used in our sensitivity analysis (Section 5.1), where the task is to optimize quantum chemical energy (QE) of planar molecules. This serves as a natural extension of our regression experiments, validating whether performance observed there translates to decision-making applications.

**3D molecules (QM9)** Since most realistic molecules are not planar, we extend our evaluation to the 3D domain using the full QM9 dataset (Ramakrishnan et al., 2014). Here, we utilize the solid harmonic wavelet scattering trans-

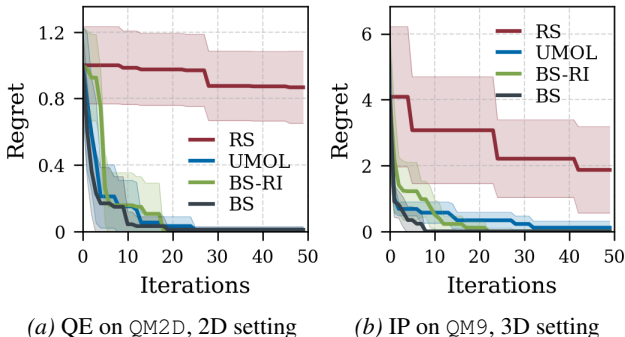


Figure 4. Regret of BO of molecular properties. Curves show the mean over 5 runs; shaded regions show 0.95 confidence intervals. In the legend, RS stands for random search, UMOL for Uni-Mol, BS for Bayesian scattering and RI for rotation-invariant.

form (Eickenberg et al., 2017; 2018), which generalizes the principles of stability and invariance to volumetric data. We optimize isotropic polarizability (IP), electronic spatial extent (ESE), and internal energy at 0K (U0).

**Setup** We employ a GP regression head. While we tested various configurations (including ESE, U0, and different kernels; see Appendix B), in the main text we restrict to Matérn- $5/2$  kernel without ARD, which yielded the most consistent performance, and IP property. We benchmark against Uni-Mol (Zhou et al., 2023), a pre-trained SE(3)-equivariant transformer designed specifically for molecular representation learning and not based on image-like representations of molecules. Starting with 50 random molecules, we perform 50 iterations of sequential selection using expected improvement acquisition optimized over a pool of 1,000 random candidates. Model hyperparameters are re-optimized at every step to adapt to the growing dataset. We report *simple regret*, defined as the difference between the true optimum and the best value found so far.

**Results** Figure 4 shows the optimization trajectories. On 2D molecules (QM2D), Bayesian scattering (BS) demonstrates remarkable efficiency, converging to near-zero regret in roughly 10 iterations while Uni-Mol requires somewhat more (Figure 4a). This performance confirms that for standard tasks involving planar geometry, a principled baseline can be surprisingly competitive. In the 3D setting (QM9), solid harmonic scattering proves equally effective (Figure 4b). Contrary to the assumption that voxel-based representations might struggle with complex quantum properties, Bayesian scattering performs on par with—and arguably converges faster than—the domain-specific Uni-Mol baseline. This demonstrates that the geometric priors encoded in the scattering transform provide a robust foundation for decision-making even in complex settings.

## 6. Conclusion

We present Bayesian scattering as a principled baseline for uncertainty quantification for images. By combining the geometric inductive biases of the scattering transform with simple probabilistic heads, it avoids the overfitting typical of learned features, fostering robustness to distribution shift. Empirically, we show that this baseline is competitive with deep learning methods in data-scarce regression and effective for downstream decision-making. We hope this work provides a rigorous foundation to ground the evaluation of future robust machine learning systems.

## References

- M. Abdar, F. Pourpanah, S. Hussain, D. Rezazadegan, L. Liu, M. Ghavamzadeh, P. Fieguth, X. Cao, A. Khosravi, U. R. Acharya, V. Makarenkov, and S. Nahavandi. A review of uncertainty quantification in deep learning: Techniques, applications and challenges. *Information Fusion*, 2021. Cited on page 1.
- M. Andreux, T. Angles, G. Exarchakis, R. Leonarduzzi, G. Rochette, L. Thiry, J. Zarka, S. Mallat, J. Andén, E. Belilovsky, J. Bruna, V. Lostanlen, M. Chaudhary, M. J. Hirn, E. Oyallon, S. Zhang, C. Cella, and M. Eickenberg. Kymatio: Scattering transforms in Python. *Journal of Machine Learning Research*, 2020. Cited on pages 4, 5.
- M. Awais, M. Naseer, S. Khan, R. M. Anwer, H. Cholakkal, M. Shah, M.-H. Yang, and F. S. Khan. Foundation models defining a new era in vision: a survey and outlook. *IEEE Transactions on Pattern Analysis and Machine Intelligence*, 2025. Cited on page 1.
- L. C. Blum and J.-L. Reymond. 970 million druglike small molecules for virtual screening in the chemical universe database GDB-13. *Journal of the American Chemical Society*, 2009. Cited on page 5.
- R. Bommasani, D. A. Hudson, E. Adeli, R. Altman, S. Arora, S. von Arx, M. S. Bernstein, J. Bohg, A. Bosselut, E. Brunskill, E. Brynjolfsson, S. Buch, D. Card, R. Castellon, N. S. Chatterji, A. S. Chen, K. A. Creel, J. Davis, D. Demszky, C. Donahue, M. Doumbouya, E. Durmus, S. Ermon, J. Etchemendy, K. Ethayarajh, L. Fei-Fei, C. Finn, T. Gale, L. E. Gillespie, K. Goel, N. D. Goodman, S. Grossman, N. Guha, T. Hashimoto, P. Henderson, J. Hewitt, D. E. Ho, J. Hong, K. Hsu, J. Huang, T. F. Icard, S. Jain, D. Jurafsky, P. Kalluri, S. Karamcheti, G. Keeling, F. Khani, O. Khattab, P. W. Koh, M. S. Krass, R. Krishna, R. Kuditipudi, A. Kumar, F. Ladhak, M. Lee, T. Lee, J. Leskovec, I. Levent, X. L. Li, X. Li, T. Ma, A. Malik, C. D. Manning, S. P. Mirchandani, E. Mitchell, Z. Munyikwa, S. Nair, A. Narayan, D. Narayanan, B. Newman, A. Nie, J. C. Niebles, H. Nilforoshan, J. F. Nyarko, G. Ogut, L. Orr, I. Papadimitriou, J. S. Park, C. Piech, E. Portelance, C. Potts, A. Raghunathan, R. Reich, H. Ren, F. Rong, Y. H. Roohani, C. Ruiz, J. Ryan, C. R’e, D. Sadigh, S. Sagawa, K. Santhanam, A. Shih, K. P. Srinivasan, A. Tamkin, R. Taori, A. W. Thomas, F. Tramèr, R. E. Wang, W. Wang, B. Wu, J. Wu, Y. Wu, S. M. Xie, M. Yasunaga, J. You, M. A. Zaharia, M. Zhang, T. Zhang, X. Zhang, Y. Zhang, L. Zheng, K. Zhou, and P. Liang. On the Opportunities and Risks of Foundation Models. *arXiv preprint arXiv:2108.07258*, 2021. Cited on page 1.
- J. Bradshaw, A. G. d. G. Matthews, and Z. Ghahramani. Adversarial examples, uncertainty, and transfer testing robustness in Gaussian process hybrid deep networks. *arXiv preprint arXiv:1707.02476*, 2017. Cited on page 2.
- J. Bruna and S. Mallat. Invariant Scattering Convolution Networks. *IEEE Transactions on Pattern Analysis and Machine Intelligence*, 35(8), 2013. Cited on pages 1–4, 6.
- T. Cohen and M. Welling. Group equivariant convolutional networks. In *International Conference on Machine Learning*, 2016. Cited on page 3.
- E. Daxberger, A. Kristiadi, A. Immer, R. Eschenhagen, M. Bauer, and P. Hennig. Laplace Redux – Effortless Bayesian Deep Learning. *Advances in Neural Information Processing Systems*, 34, 2021. Cited on page 2.
- A. Dosovitskiy, L. Beyer, A. Kolesnikov, D. Weissenborn, X. Zhai, T. Unterthiner, M. Dehghani, M. Minderer, G. Heigold, S. Gelly, J. Uszkoreit, and N. Houlsby. An Image is Worth 16x16 Words: Transformers for Image Recognition at Scale. In *International Conference on Learning Representations*, 2020. Cited on page 1.
- M. Eickenberg, G. Exarchakis, M. Hirn, and S. Mallat. Solid harmonic wavelet scattering: Predicting quantum molecular energy from invariant descriptors of 3D electronic densities. In *Advances in Neural Information Processing Systems*, 2017. Cited on pages 1, 2, 4, 8.
- M. Eickenberg, G. Exarchakis, M. Hirn, S. Mallat, and L. Thiry. Solid harmonic wavelet scattering for predictions of molecule properties. *The Journal of Chemical Physics*, 2018. Cited on page 8.
- K. Ferkous, F. Chellali, A. Kouzou, and B. Bekkar. Wavelet-Gaussian process regression model for forecasting daily solar radiation in the Saharan climate. *Clean Energy*, 5(2), 2021. Cited on page 2.
- P. I. Frazier. A tutorial on Bayesian optimization. *arXiv preprint arXiv:1807.02811*, 2018. Cited on page 8.

- Y. Gal and Z. Ghahramani. Dropout as a bayesian approximation: Representing model uncertainty in deep learning. In *International Conference on Machine Learning*, 2016. Cited on page 2.
- S. Gauthier, B. Thérien, L. Alsene-Racicot, M. Chaudhary, I. Rish, E. Belilovsky, M. Eickenberg, and G. Wolf. Parametric scattering networks. In *IEEE/CVF Conference on Computer Vision and Pattern Recognition*, 2022. Cited on page 1.
- J. Gawlikowski, C. R. N. Tassi, M. Ali, J. Lee, M. Humt, J. Feng, A. Kruspe, R. Triebel, P. Jung, R. Roscher, M. Shahzad, W. Yang, R. Bamler, and X. X. Zhu. A survey of uncertainty in deep neural networks. *Artificial Intelligence Review*, 2023. Cited on page 1.
- S. Graham, Q. D. Vu, S. E. A. Raza, A. Azam, Y. W. Tsang, J. T. Kwak, and N. Rajpoot. Hover-net: Simultaneous segmentation and classification of nuclei in multi-tissue histology images. *Medical Image Analysis*, 2019. Cited on page 7.
- F. K. Gustafsson, M. Danelljan, and T. B. Schön. How Reliable is Your Regression Model’s Uncertainty Under Real-World Distribution Shifts? *Transactions on Machine Learning Research*, 2023. Cited on pages 1, 2, 6.
- J. Hensman, N. Fusi, and N. D. Lawrence. Gaussian Processes for Big Data. In *Uncertainty in Artificial Intelligence*, 2013. Cited on pages 5, 7.
- M. Hirn, S. Mallat, and N. Poilvert. Wavelet scattering regression of quantum chemical energies. *Multiscale Modeling & Simulation*, 15(2), 2017. Cited on pages 1, 2, 4, 5, 12.
- D. P. Kingma. Adam: A method for stochastic optimization. *arXiv preprint arXiv:1412.6980*, 2014. Cited on page 6.
- P. W. Koh, S. Sagawa, H. Marklund, S. M. Xie, M. Zhang, A. Balsubramani, W. Hu, M. Yasunaga, R. L. Phillips, I. Gao, T. Lee, E. David, I. Stavness, W. Guo, B. A. Earnshaw, I. S. Haque, S. Beery, J. Leskovec, A. Kundaje, E. Pierson, S. Levine, C. Finn, and P. Liang. WILDS: A Benchmark of in-the-Wild Distribution Shifts. In *International Conference on Machine Learning*, 2021. Cited on pages 1, 2, 6, 7.
- B. Lakshminarayanan, A. Pritzel, and C. Blundell. Simple and scalable predictive uncertainty estimation using deep ensembles. *Advances in Neural Information Processing Systems*, 2017. Cited on page 2.
- A. W. Lone and N. Aydin. Wavelet scattering transform based doppler signal classification. *Computers in Biology and Medicine*, 167, 2023. Cited on page 2.
- D. J. C. MacKay. Bayesian Interpolation. *Neural Computation*, 4(3), 1992. Cited on page 6.
- S. Mallat. Group invariant scattering. *Communications on Pure and Applied Mathematics*, 65, 2012. Cited on pages 3, 4, 12.
- S. Mallat. Recursive interferometric representation. In *EU-SICO conference*, 2010. Cited on page 1.
- P. Naylor, M. Laé, F. Reyal, and T. Walter. Segmentation of nuclei in histopathology images by deep regression of the distance map. *IEEE transactions on medical imaging*, 2018. Cited on page 7.
- S. Ojha, N. Jangid, A. Shelke, and A. Habib. Probabilistic impact localization in composites using wavelet scattering transform and multi-output Gaussian process regression. *Measurement*, 2024. Cited on page 2.
- Y. Ovadia, E. Fertig, J. Ren, Z. Nado, D. Sculley, S. Nowozin, J. Dillon, B. Lakshminarayanan, and J. Snoek. Can You Trust Your Model’s Uncertainty? Evaluating Predictive Uncertainty Under Dataset Shift. In *Advances in Neural Information Processing Systems*, 2019. Cited on page 2.
- E. Oyallon, S. Zagoruyko, G. Huang, N. Komodakis, S. Lacoste-Julien, M. Blaschko, and E. Belilovsky. Scattering networks for hybrid representation learning. *IEEE Transactions on Pattern Analysis and Machine Intelligence*, 41(9), 2018. Cited on pages 1, 2.
- R. Ramakrishnan, P. O. Dral, M. Rupp, and O. A. von Lilienfeld. Quantum chemistry structures and properties of 134 kilo molecules. *Scientific Data*, 2014. Cited on pages 2, 8.
- C. E. Rasmussen and C. K. I. Williams. *Gaussian Processes for Machine Learning*. MIT Press, 2006. Cited on pages 1, 5, 6.
- L. Ruddigkeit, R. Van Deursen, L. C. Blum, and J.-L. Reymond. Enumeration of 166 billion organic small molecules in the chemical universe database GDB-17. *Journal of Chemical Information and Modeling*, 2012. Cited on page 2.
- M. Rupp, A. Tkatchenko, K.-R. Müller, and O. A. Von Lilienfeld. Fast and accurate modeling of molecular atomization energies with machine learning. *Physical Review Letters*, 108(5), 2012. Cited on page 5.
- S. Sudirman, F. Natalia, A. Sophian, and A. Ashraf. Pulsed Eddy Current signal processing using wavelet scattering and Gaussian process regression for fast and accurate ferromagnetic material thickness measurement. *Alexandria Engineering Journal*, 61(12), 2022. Cited on page 2.

- K. Tran, W. Neiswanger, J. Yoon, Q. Zhang, E. Xing, and Z. W. Ulissi. Methods for comparing uncertainty quantifications for material property predictions. *Machine Learning: Science and Technology*, 2020. Cited on page 7.
- P. Tschandl, C. Rosendahl, and H. Kittler. The HAM10000 dataset, a large collection of multi-source dermatoscopic images of common pigmented skin lesions. *Scientific data*, 2018. Cited on page 6.
- I. Waldspurger. Exponential decay of scattering coefficients. In *International Conference on Sampling Theory and Applications*, 2017. Cited on page 4.
- A. G. Wilson, Z. Hu, R. Salakhutdinov, and E. P. Xing. Deep kernel learning. In *Artificial Intelligence and Statistics*, 2016. Cited on page 2.
- C. Yeh, A. Perez, A. Driscoll, G. Azzari, Z. Tang, D. Lobell, S. Ermon, and M. Burke. Using publicly available satellite imagery and deep learning to understand economic well-being in Africa. *Nature Communications*, 2020. Cited on pages 2, 7.
- G. Zhou, Z. Gao, Q. Ding, H. Zheng, H. Xu, Z. Wei, L. Zhang, and G. Ke. Uni-mol: A universal 3d molecular representation learning framework. In *International Conference on Learning Representations*, 2023. Cited on page 8.

## A. Scattering Transforms

### A.1. Failure Modes in Satisfying the Properties from Section 3.1

Constructing feature maps that are simultaneously invariant, stable, and expressive is a nontrivial challenge. Naïve choices often fail to balance these:

- The identity map  $\Phi(f) = f$  is maximally expressive, but lacks translation-invariance.
- Canonical invariants—such as aligning an image based on its maximum—achieve translation-invariance, but become highly unstable to small deformations or additive noise.
- The absolute value of the Fourier transform is also translation-invariant, and stable to additive noise, but—as shown in Mallat (2012)—is *not* stable to small deformations.
- Convolutions can be made stable to small deformations and additive noise, but they are translation-equivariant ( $\Phi(T_c f) = T_c \Phi(f)$ ) rather than invariant ( $\Phi(T_c f) = \Phi(f)$ ).
- Globally pooling equivariant features such as convolutions, e.g. by averaging, produces invariance but often at the expense of expressivity, potentially discarding crucial information.

These examples illustrate the tension between invariance, stability, and richness in feature design. The wavelet scattering transform resolves this trade-off by interleaving convolution, non-linearity, and averaging in a principled cascade, yielding features that provably satisfy all three desiderata.

## B. Additional Experimental Details

In this appendix, we report the additional results for the different scenarios evaluated in the paper, as well as provide more details of experimental setups.

### B.1. Sensitivity Analysis and Best Practices

As discussed in Section 5.1, an extensive empirical evaluation was conducted to study the sensitivity of Bayesian scattering to various design choices and come up with best practices. Taking inspiration from Hirn et al. (2017), we used a subset of the QM7 dataset of small molecules consisting of only planar molecules for these tests. The resulting dataset comprises a total of 4,357 molecules and is termed QM2D below. Following the methodology of Hirn et al. (2017), for each molecule we generated a 2D image representation with three channels corresponding to the electronic density of the valence electrons, core electrons, and to the *dirac* channel which places atomic charge values at the locations of the respective nuclei.

The files QM2D\_1---5.pdf in <https://github.com/nash169/bayesian-scattering/tree/main/results> report a range of experiments designed to study the sensitivity of model performance to various design choices. Specifically, we analyze the impact of: (1) training set size and number of training iterations; (2) scattering transform hyperparameters, i.e., the number of scales  $J$  and the number of angular orientations  $L$ ; (3) number of input channels; (4) image resolution; (5) application of PCA to the scattering features.

Complementing the analysis in Section 5.1, we observe that increasing the number of input channels consistently improves performance, as expected given the additional information they provide. Notably, however, the valence channel emerges as the most influential input. This aligns with chemical intuition, suggesting that valence interactions are the primary determinants of the relevant molecular properties. We omit these details from the main text because channel importance—while a valid sanity check—is highly specific to this dataset and offers limited generalizable insight.

### B.2. Image Regression

Detailed tabulated results for the image regression experiments are provided in the file `dist-shift-exact-gp.pdf` in <https://github.com/nash169/bayesian-scattering/tree/main/results>. In this section, we provide a dataset-specific analysis of the performance trends and hyperparameter sensitivity. For all image regression tasks, we employed a consistent evaluation protocol: images were resized to  $64 \times 64$  pixels (allowing a maximum scattering scale  $J = 6$ ), and models were trained on 1000 points and evaluated on 250 points using 5 (potentially intersecting) splits

randomly subsampled from the dataset and subordinate to the dataset-predefined split (train is subsampled from the train part only, test is subsampled from the test part only, where the original train and test parts exhibit a shift), with splits synchronized across all methods. We evaluated scattering transforms with  $L = 8$  angles, considering both standard and rotation-invariant features coupled with RBF and Matérn kernels (with and without ARD).

### B.2.1. SKINLESIONPIXELS DATASET

For this dataset, we evaluated scattering scales  $J \in \{3, 4, 5\}$ . For each scale we evaluated rotation covariant and invariant scattering features.

**Performance Analysis.** On the skin lesion task, Bayesian scattering remains competitive but presents a distinct trade-off profile compared to the neural features. Interestingly, DinoV2 performs worse on this task by virtually all accounts.

- **RMSE:** Scattering achieves an RMSE comparable to both ConvNeXt Base and ConvNeXt Atto but is considerably better than DinoV2.
- **NLL:** Scattering achieves an NLL that is worse but comparable to ConvNeXt Base, while outperforming ConvNeXt Atto. The NLL of DinoV2 is considerably worse.
- **Calibration (QCE):** In terms of calibration error, scattering is strictly worse than ConvNeXt Base (statistically significant) and on par with ConvNeXt Atto. DinoV2 is considerably worse than scattering in QCE.
- **Prediction Intervals:** Despite the somewhat higher QCE, scattering exhibits desirable uncertainty characteristics for decision-making. Its prediction intervals are much narrower than those of ConvNeXt Base, yet they exhibit significantly higher variance from point to point. This variability suggests the model is selectively uncertain, whereas ConvNeXt Base tends to output broad, uniform intervals regardless of input difficulty.

**Model Selection and Sensitivity.** In contrast to the histology dataset, performance here is highly sensitive to hyperparameters. Rotation-invariant scattering with  $J = 3$  ( $L = 8$ ) performs significantly better than all other scattering configurations. Regarding the probabilistic head, non-ARD kernels consistently outperform ARD versions, while the choice between RBF and Matérn kernels has negligible impact. This dataset also provides a clear example where training objectives fail to predict test performance: ConvNeXt Base yielded one of the highest (worst) training losses ( $0.948 \pm 0.053$ ) yet achieved the best test NLL, confirming that model selection based on training loss is unreliable here. Finally, although ensembles as probabilistic heads achieve top performance in mean prediction here, they suffer from massive overconfidence.

### B.2.2. HISTOLOGYNUCLEIPIXELS DATASET

For this dataset, we evaluated scattering scales  $J \in \{3, 4, 5\}$ . For each scale we evaluated rotation covariant and invariant scattering features.

**Performance Analysis.** Bayesian scattering demonstrates top-tier performance on the histology dataset, matching or exceeding the results of neural features across both deterministic and probabilistic metrics.

- **RMSE:** Scattering achieves an RMSE on par with both DinoV2 variants and strictly outperforms ConvNeXt.
- **NLL:** In terms of negative log-likelihood, scattering is generally superior or comparable to all neural network models.
- **Calibration (QCE):** Scattering shows strong calibration; its QCE is comparable to the best-performing neural model (ConvNeXt Atto) and is significantly better than the rest of neural features.
- **Prediction Intervals:** Regarding the geometry of uncertainty, scattering produces prediction intervals that are narrower (more informative) than competitors for the respective QCE levels. However, on the other hand, the standard deviation of these interval widths is relatively small across the test set.

Table 3. Performance comparison on the full datasets using SVGP inference. We report mean and standard deviation across 5 training runs on the fixed full split. Best results are underlined; those not statistically distinguishable are **bolded**.

Data	Metric	Trivial	Scattering	ConvNeXt		DINOv2	
				Atto	Base	Small	Base
SLP	RMSE	817 ± 35	<b>540 ± 33</b>	<u>515 ± 39</u>	<b>556 ± 21</b>	748 ± 56	687 ± 40
	NLL	1.50 ± 0.05	<b>1.16 ± 0.12</b>	<u>1.13 ± 0.13</u>	<b>1.15 ± 0.07</b>	1.46 ± 0.12	1.40 ± 0.10
	QCE	0.03 ± 0.01	0.08 ± 0.02	0.08 ± 0.02	<b>0.06 ± 0.02</b>	0.10 ± 0.02	0.10 ± 0.02
	PI- $\mu$	3.92 ± 0.00	<u>1.84 ± 0.01</u>	1.93 ± 0.01	2.32 ± 0.05	2.71 ± 0.08	2.50 ± 0.09
	PI- $\sigma$	0.00 ± 0.00	0.11 ± 0.00	0.09 ± 0.01	0.07 ± 0.01	0.13 ± 0.01	0.17 ± 0.04
HP	RMSE	623 ± 14	<b>375 ± 12</b>	451 ± 25	481 ± 26	421 ± 19	<b>392 ± 20</b>
	NLL	1.31 ± 0.02	<b>0.82 ± 0.02</b>	0.87 ± 0.03	0.92 ± 0.03	<b>0.84 ± 0.03</b>	<b>0.77 ± 0.04</b>
	QCE	0.05 ± 0.00	0.02 ± 0.01	0.03 ± 0.01	0.03 ± 0.01	<b>0.00 ± 0.01</b>	<b>0.00 ± 0.01</b>
	PI- $\mu$	3.92 ± 0.00	2.56 ± 0.00	2.45 ± 0.03	2.58 ± 0.03	2.55 ± 0.03	<b>2.36 ± 0.03</b>
	PI- $\sigma$	0.00 ± 0.00	0.02 ± 0.00	0.05 ± 0.01	0.06 ± 0.00	0.11 ± 0.03	0.12 ± 0.01
AW	RMSE	0.90 ± 0.02	0.56 ± 0.04	<b>0.50 ± 0.01</b>	<b>0.50 ± 0.03</b>	<b>0.49 ± 0.01</b>	<b>0.49 ± 0.01</b>
	NLL	1.54 ± 0.03	0.96 ± 0.05	<b>0.86 ± 0.02</b>	<b>0.88 ± 0.05</b>	<b>0.87 ± 0.03</b>	<b>0.87 ± 0.03</b>
	QCE	0.01 ± 0.01	0.01 ± 0.01	<b>0.01 ± 0.01</b>	<b>0.01 ± 0.01</b>	<b>0.01 ± 0.01</b>	<b>0.01 ± 0.01</b>
	PI- $\mu$	3.92 ± 0.00	2.79 ± 0.06	<b>2.30 ± 0.01</b>	2.42 ± 0.02	2.34 ± 0.01	<b>2.28 ± 0.01</b>
	PI- $\sigma$	0.00 ± 0.00	0.10 ± 0.03	0.08 ± 0.00	0.03 ± 0.00	0.04 ± 0.00	0.04 ± 0.00

**Model Selection and Sensitivity.** Performance on this dataset is highly robust to hyperparameter variations. Metrics (excluding PI statistics) are largely insensitive to the scattering scale  $J$ , the use of rotation invariance, the choice of kernel (RBF vs. Matérn), or the use of ARD. Minor differences appear only in PI statistics, where we observe a slight preference for  $J = 5$  without rotation invariance using an RBF kernel (regardless of ARD). Training marginal likelihood values were very comparable across models, making them an ineffective metric for model selection. Finally, using ensembles as probabilistic heads proved detrimental, yielding worse performance across all metrics compared to alternative using Gaussian processes.

### B.2.3. ASSETWEALTH DATASET

For scattering, we resized the images to  $256 \times 256$ , and evaluated scattering scales  $J \in \{5, 6, 7\}$ . For each scale we evaluated rotation covariant and invariant scattering features.

**Performance Analysis.** In this domain, Bayesian scattering generally lags behind learned features.

- **RMSE:** Scattering yields significantly higher error than both ConvNeXt and DinoV2 variants.
- **NLL:** In terms of negative log-likelihood, scattering performs comparably to ConvNeXt but is significantly outperformed by DinoV2.
- **Calibration (QCE):** Despite lower predictive accuracy, the calibration of Bayesian scattering remains robust, achieving QCE scores comparable to both ConvNeXt and DinoV2.
- **Prediction Intervals:** Scattering tends to produce wider, less informative prediction intervals compared to the neural baselines, although the dispersion (standard deviation) of interval widths is slightly more favorable.

**Model Selection and Sensitivity.** Hyperparameter choices play a critical role here. We find that ARD is highly detrimental to scattering performance, likely due to overfitting in the high-dimensional feature space. Conversely, enforcing rotation invariance proves beneficial. Regarding metric reliability, training marginal likelihood is misleading when ARD is included, as it favors the overfitting ARD models (low train loss, high test loss). However, if ARD configurations are excluded, the training loss correctly identifies that neural network features are superior to scattering features, aligning with test performance. Finally, consistent with other tasks, deep ensembles provide reasonable mean predictions but fail to deliver reliable uncertainty estimates.

### B.2.4. MORE DATA AND APPROXIMATE INFERENCE

To assess scalability and performance on larger datasets, we employ SVGP inference. We conduct this evaluation on the three image regression datasets considered. The results are summarized in Table 3. Detailed tabulated results are provided in the file `dist-shift-svgp.pdf` in <https://github.com/nash169/bayesian-scattering/tree/main/results>. Note that unlike the experiments in the main text, the the train test here is fixed; thus, the reported variance across 5 seeds arises from the stochastic optimization, initialization, and randomness in test set subsampling (we chose 250 random test points out of the whole test set for every trial).

### B.3. Bayesian Optimization

Regret plots for Bayesian optimization with different probabilistic heads can be found in Figure 5.

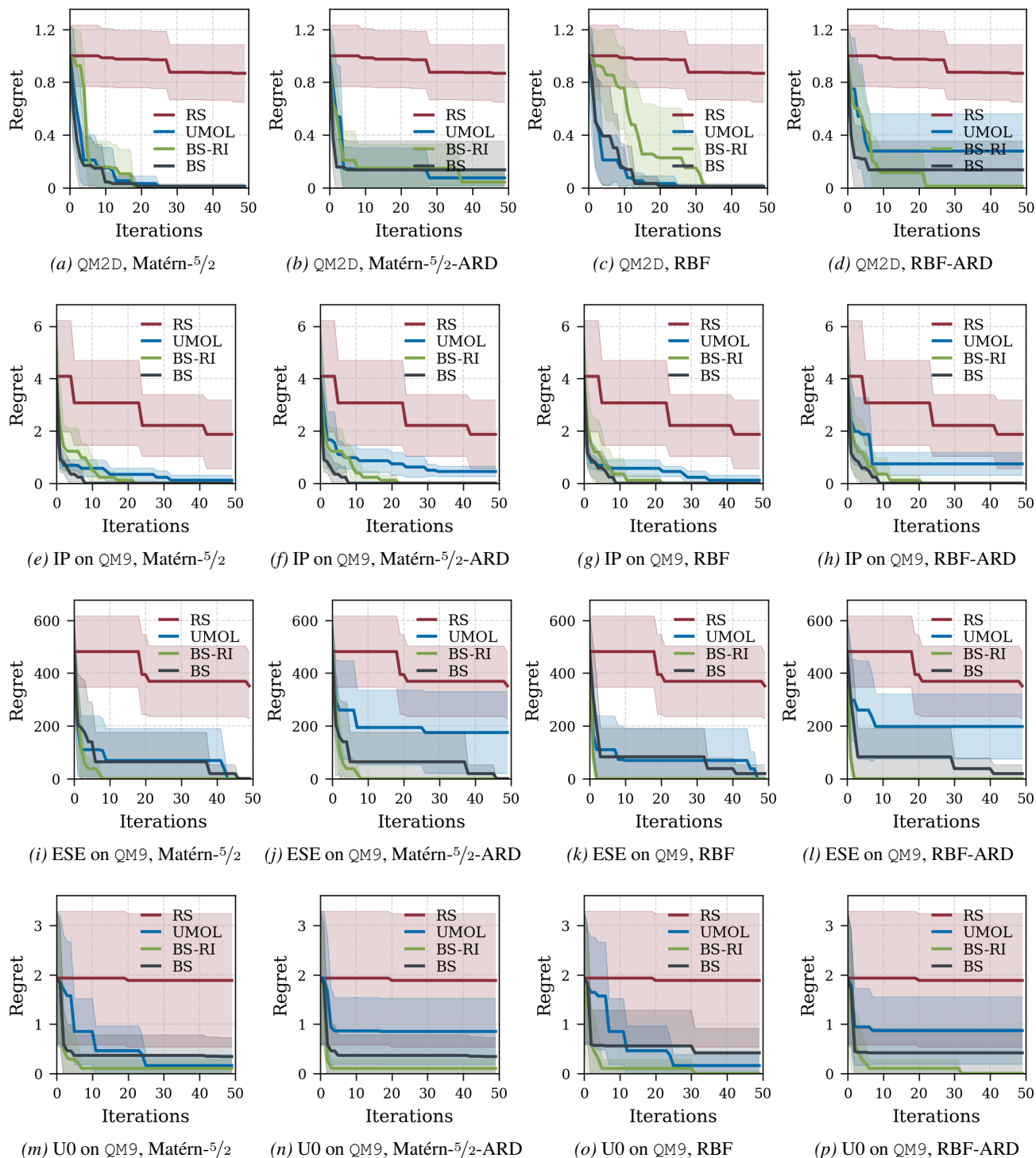


Figure 5. Molecular property BO (extended). Curves show the mean regret over 5 runs; shaded regions show 0.95 confidence intervals.